Advanced Materials

ADVANCED MATERIALS
www.advmat.de

RESEARCH ARTICLE

Rapid Identification of Nanoscale Point Defects in Two-Dimensional Crystals by Rare-Earth-Enhanced Fluorescence

Tianyao Liu[1,2] | Wenya Wei[3] | Mingchao Ding[1] | Pan Wu[1] | Ruixi Qiao[4] | Quanlin Guo[2] | Zhibin Zhang[2] | Mengze Zhao[2] | Peng Yin[5] | Can Liu[5] | Hao Hong[2] | Xiaozhi Xu[3] | Kaihui Liu[2] | Xuedong Bai[1] | Li Wang[1]

[1]Beijing National Laboratory for Condensed Matter Physics, Institute of Physics, Chinese Academy of Sciences, Beijing, China | [2]State Key Laboratory for Mesoscopic Physics, School of Physics, Peking University, Beijing, China | [3]Guangdong Provincial Key Laboratory of Quantum Engineering and Quantum Materials, Guangdong-Hong Kong Joint Laboratory of Quantum Matter, School of Physics, South China Normal University, Guangzhou, China | [4]State Key Laboratory of Mechanics and Control of Mechanical Structures, Key Laboratory for Intelligent Nano Materials and Devices of the Ministry of Education, Institute for Frontier Science, Nanjing University of Aeronautics and Astronautics, Nanjing, China | [5]Department of Physics, Renmin University of China, Beijing, China

Correspondence: Li Wang (liwang@iphy.ac.cn)

Received: 7 March 2026 | **Revised:** 20 June 2026 | **Accepted:** 9 July 2026

Keywords: 2D materials | photoluminescence | point defects | rare earth

ABSTRACT

Identifying nanoscale point defects (NPDs) is essential for producing high-quality two-dimensional (2D) crystals and moving them towards scalable device integration. However, existing methods face a fundamental compromise between spatial resolution and detection throughput: atomic-resolution techniques provide limited testing area or sampling rates, whereas conventional optical methods often lack sufficient sensitivity required for low-density NPDs. Here, we present a highly sensitive, non-destructive strategy that employs erbium chloride ($ErCl_3$) to form erbium-rich nanoparticles (Er-NPs) as fluorescent markers at NPD sites on 2D crystal surfaces, enabling rapid and precise mapping of NPDs in large-area samples. Both theoretical modeling and experimental observations demonstrate that Er-NPs preferentially accumulate at defect sites, substantially enhancing localized photoluminescence (PL) signals and enabling direct visualization of NPD locations and distributions. This approach complements established optical techniques, including Raman spectroscopy, by providing higher-contrast and more efficient localization of low-density nanoscale defects across large-area samples. Importantly, Er-NPs can be fully removed through annealing under ultrahigh vacuum (UHV), ensuring the non-destructive nature of the method. This work provides a powerful tool for quality control of 2D materials, supporting their transition from laboratory synthesis to large-scale industrial applications.

1 | Introduction

Two-dimensional (2D) materials have attracted extensive research interest owing to their exceptional properties and tremendous potential for next-generation electronic and optoelectronic devices. Recent advances in synthesizing large-area, high-quality 2D single crystals have opened opportunities for integrated 2D devices with superior performance [1–5]. In this context, assessing the quality of these 2D films is particularly important. Typically, grain boundaries are absent in high-quality single

Tianyao Liu, Wenya Wei, and Mingchao Ding contributed equally to this work.

crystals produced by seamless stitching of multiple domains with uniform lattice orientations [6–9]. Even when such line defects emerge, they can be identified by nonlinear optical techniques such as polarization-resolved second-harmonic generation (SHG) [10–12]. In contrast, nanoscale point defects (NPDs) commonly exist even in the highest-quality 2D single crystals and degrade essential material properties and device performance [13, 14]. Therefore, rapid and accurate identification of NPDs is highly desired to bridge the critical gap between large-area synthesis and practical applications of 2D materials in the current situation.

Techniques for detecting NPDs in 2D materials generally fall into three categories: (i) direct atomic-scale imaging, such as transmission electron microscopy (TEM) [15–21], scanning tunnelling microscopy (STM) [22–26], and atomic force microscopy (AFM) [27]; (ii) optical spectroscopic characterizations, including Raman spectroscopy [28–30], photoluminescence (PL) [31–33], and SHG [34]; and (iii) visualization methods involving special pre-treatments. Each approach has inherent limitations. Specifically, atomic-scale imaging provides direct visualization of defect locations, types, and densities, but it typically requires complex sample preparation and strict environmental conditions, limiting the spatial coverage and sampling efficiency. Conversely, optical spectroscopy techniques offer higher throughput but often suffer from insufficient sensitivity to low-density NPDs, yielding negligible signal responses. Pre-treatment-based detection methods, such as ultraviolet irradiation [35], selective etching [36–40], and liquid coatings [41, 42], have shown promise but frequently induce irreversible structural damage or introduce additional defects, compromising measurement accuracy. Consequently, developing a high-throughput, highly sensitive, and non-destructive approach for identifying NPDs in high-quality, large-area 2D single crystals remains a substantial challenge.

In our design, rare-earth-based fluorescent materials offer distinct advantages as "markers" for non-destructive NPD detection in 2D materials. Rare-earth ions exhibit ultra-narrow emission lines and large Stokes shifts, enabling high signal-to-noise ratios (SNR) for spectral identification. In addition, rare-earth nanoparticles show exceptional photostability and maintain stable luminescence under prolonged excitation compared with conventional organic dyes or quantum dots. Specifically, we select rare-earth compound erbium chloride ($ErCl_3$) for adsorption at NPD sites, due to its relatively low evaporation temperature, cost-effectiveness (compared to other rare-earth compounds), and strong fluorescence characteristics. A low-pressure tube furnace with a modulated temperature gradient is utilized to achieve controllable deposition of an optimized amount of Er-rich nanoparticles (Er-NPs) derived from $ErCl_3$ onto 2D material surfaces (graphene serves as a representative system to elucidate the underlying mechanisms) (Figure 1). Combined theoretical and experimental results demonstrate that Er-NPs preferentially adsorb at NPD sites in 2D materials, significantly enhancing local fluorescence signals. This selective adsorption enables rapid identification of NPD positions via PL imaging, providing high-efficiency defect localization and large-area screening capabilities. Importantly, our technique has minimal impact on intrinsic properties of the test material, as the adsorbed Er-NPs can be completely removed by annealing under ultrahigh vacuum (UHV) conditions following the defect characterization.

2 | Results and Discussion

Theoretical support for this approach is established through density functional theory (DFT) calculations that analyze the adsorption energetics of erbium (Er) atoms on graphene with various defect configurations. Typically, stable NPDs in 2D materials are often associated with atomic vacancies and manifest as non-hexagonal ring configurations. According to the number of missing atoms, these defects can be categorized into V_0 (vacancy-free; Stone–Wales defects), V_2 (two-atom vacancies; e.g., 5–8–5, 555–777, and 5555–7777), and V_n (multi-vacancy defects). Vacancies with an odd number of missing atoms are rarely observed because their formation is energetically less favorable [43]. The calculations show that adsorption energies become significantly more favorable for Er atoms interacting with larger defect structures. Specifically, the Stone–Wales defect, characterized by two five-membered and two seven-membered rings (55–77) [44], exhibits enhanced adsorption energy relative to pristine graphene hexagonal lattices (Figures 2a, S1, S2a). Similarly, energetically favorable adsorption occurs at common V_2 defects, including the 5–8–5, 5555–7777, and 555–777 configurations (Figures 2a and S2b–d). Notably, defects with close effective areas (e.g., 55–77 vs. 5–8–5; 5555–7777 vs. 555–777) show similar adsorption trends as Er loading increases. This result indicates that the defect area, rather than specific ring configuration or number of missing atoms, is predominant in the adsorption behaviors.

To further confirm this area dependence, we investigate the scenario of larger multi-vacancy defects (V_n) constructed from 2^n times the stable 555–777 configuration (lowest formation energy among common V_2 defects, Figure S3). Consistently, adsorption-energy calculations reveal stronger Er accumulation at larger defect sites (Figures 2b and S4), and this trend remains robust across different Er atom loading densities. Therefore, Er-NPs can act as sensitive and selective fluorescent markers for NPDs by preferentially accumulating at defect sites, translating the spatial distribution of NPDs into detectable fluorescence signals (Figure 2c). Accordingly, the Er-related PL intensity should be regarded as a readout of the effective defect area and local defect density that enable Er accumulation, rather than as a direct count of individual atomic vacancies. This capability enables efficient, high-precision mapping of defect distributions across large-area samples, addressing key needs in scalable quality control for 2D materials.

As Er^{3+} ions possess multiple well-defined energy levels, their PL typically exhibits multiple emission lines; we therefore preselect the strongest one for tracking. The most intense PL emissions occur at 556 and 672 nm, corresponding to the photons from the transitions of $^4S_{3/2} \rightarrow {}^4I_{15/2}$ and $^4F_{9/2} \rightarrow {}^4I_{15/2}$, respectively [45]. In contrast, graphene shows sharp Raman peaks near 561 and 598 nm under 514 nm excitation, corresponding to the G and 2D modes, respectively [29] (Figure S5a). Owing to the possible spectral overlap between the PL peak at 556 nm and the Raman G peak at 561 nm, the PL emission at 672 nm is selected here as the characteristic signal for NPD detection. Besides, to avoid fluorescence self-quenching at high loading (e.g., via resonant energy transfer), we perform dosage-dependent tests to determine optimized precursor dosage for accurate NPD characterization (Figure S5b).

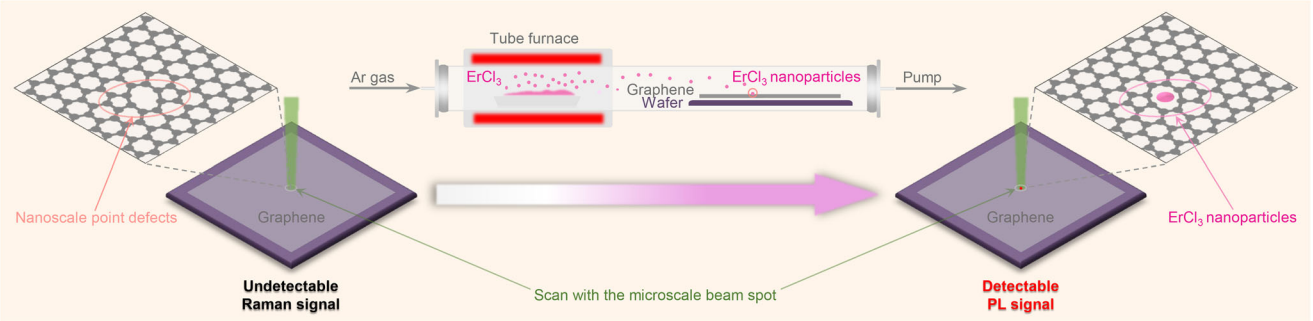

FIGURE 1 | Schematic illustration of NPD detection enabled by Er-NPs. $ErCl_3$ powder precursor is placed in the upstream high-temperature zone of a tube furnace, while the graphene sample is positioned downstream in a lower-temperature zone under Ar flow. Upon heating, $ErCl_3$ evaporates and is transported to the graphene surface, where it preferentially accumulates at NPD sites to form Er-NPs. The resulting Er-NPs generate strong and characteristic PL, converting otherwise Raman-undetectable NPDs into readily observable signals in PL mapping with a microscale excitation spot.

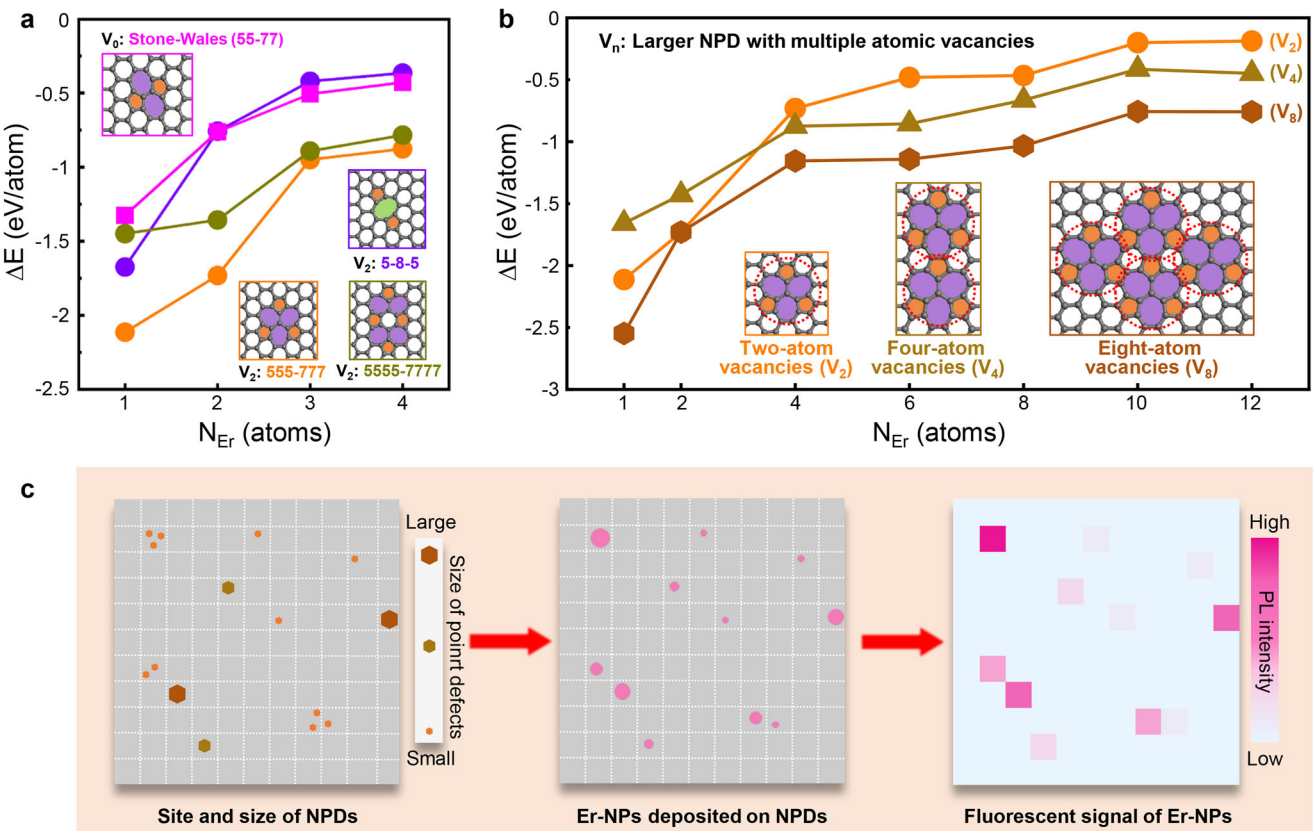

FIGURE 2 | DFT-calculated adsorption energetics of Er at graphene NPDs and the corresponding selective-adsorption mechanism for PL mapping. (a) Adsorption energy difference per Er atom (ΔE, referenced to pristine graphene) as a function of the number of adsorbed Er atoms (N_{Er}) for vacancy-free defects (V_0, Stone–Wales 55–77) and two-atom vacancy defects (V_2, 5–8–5, 555–777, and 5555–7777). (b) ΔE versus N_{Er} for larger multi-vacancy defects (V_n), exemplified by V_2, V_4, and V_8. In both (a) and (b), ΔE becomes less negative and gradually approaches saturation as N_{Er} increases, and larger defect sites yield more favourable Er adsorption. Insets show the relaxed atomic configurations of the corresponding defect structures. (c) Schematic illustration of the working principle: the locations and effective sizes of NPDs are converted into spatially resolved PL contrast through preferential accumulation of Er-NPs at defect sites.

Under these optimized conditions, we further experimentally validate this proposed approach. Nanoscale defects are intentionally introduced into pristine monolayer graphene using focused femtosecond laser pulses. The laser spot is precisely confined, and both laser power and exposure time are carefully tuned to generate irradiated zones with different damage. AFM topography reveals these irradiated regions through distinct laser footprints (Figure S5c). High-resolution TEM (HRTEM) acquired from irradiated regions confirms that laser-generated defects are typically isolated nanoscale vacancies (Figure 3a). In graphene, the Raman D band is commonly associated with the disordered sp^2-hybridized lattice induced by point defects. However, only one

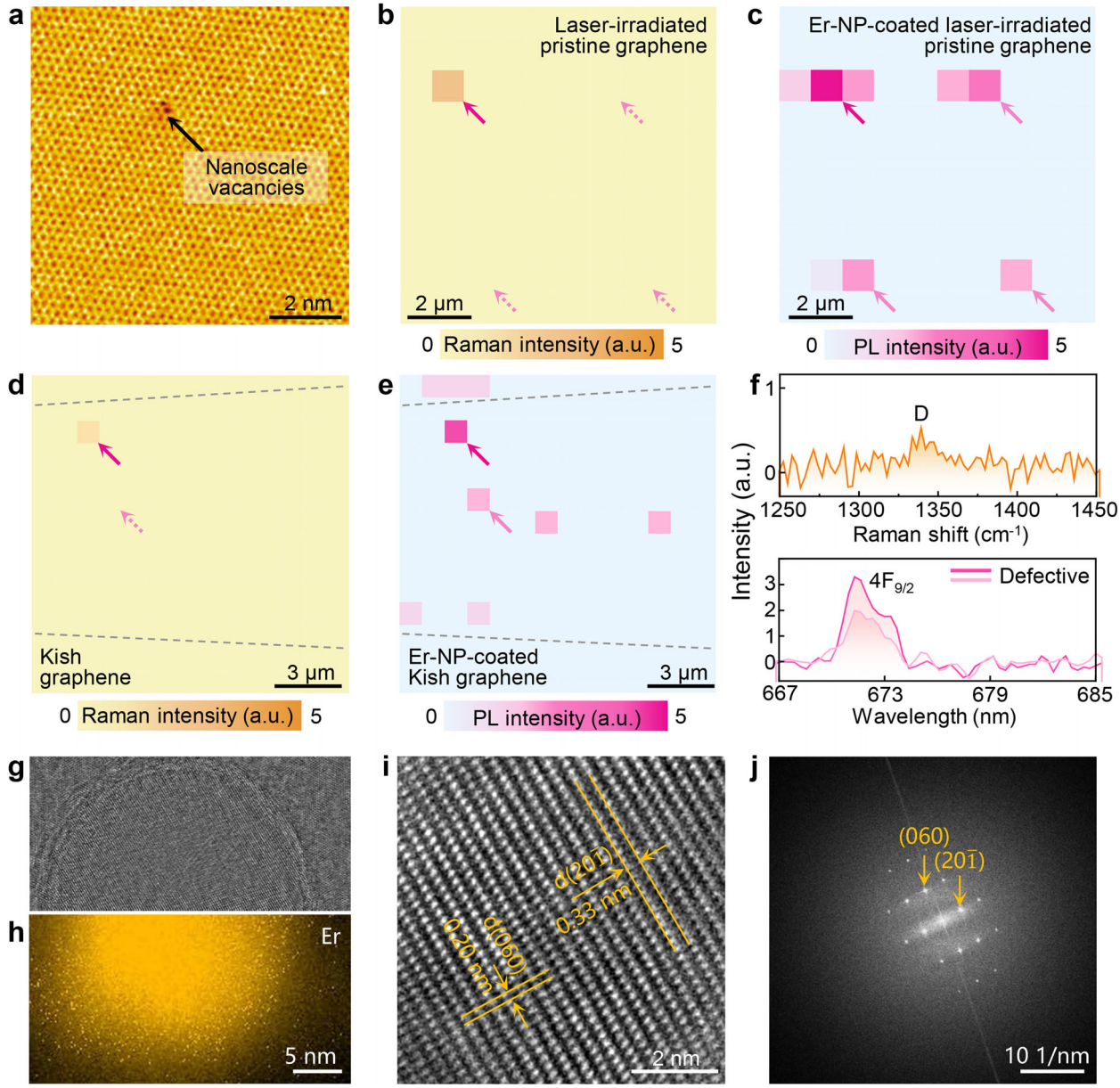

FIGURE 3 | Optical identification of NPDs in graphene through the Er-NP-assisted PL scanning. (a) HRTEM image of a laser-irradiated region, revealing isolated nanoscale vacancies. (b) Raman mapping (1345 cm^{-1}) from four laser-irradiated sites shows that only one site exhibits a discernible D band, highlighting the limited sensitivity of Raman spectroscopy for low-density NPDs. (c) PL mapping (672 nm) after Er-NP deposition shows clear fluorescence responses from all four laser-irradiated sites; the four quadrants correspond to laser powers of 75 mW (upper left), 70 mW (upper right), 65 mW (lower left), and 60 mW (lower right), and the PL intensity increases with the irradiation dose. (d) Raman D-band (1345 cm^{-1}) mapping of exfoliated Kish graphene, where only a weak localized response is observed. (e) Corresponding PL map after Er-NP deposition reveals additional localized defect-related hotspots compared with (d). (f) Raman spectra acquired from the defective region indicated in (d), with the weak D band highlighted. The bottom panel shows PL spectra collected at the two defect sites marked by the coloured arrows in (e), corresponding to a Raman-detectable location in the D-band mapping (upper trace; stronger PL) and a Raman-undetectable location (lower trace; weaker yet discernible PL), respectively. (g) HRTEM image of an individual Er-NP deposited on graphene. (h) Energy-dispersive X-ray spectroscopy elemental mapping of the individual Er-NP shown in (g), confirming pronounced Er enrichment within the nanoparticle. (i) Magnified HRTEM acquired from the interior of an Er-NP showing well-resolved lattice fringes with measured d spacings of ~0.33 and ~0.20 nm, which are consistent with the (20$\bar{1}$) and (060) planes of monoclinic $ErCl_3$ (space group C2/m), respectively. (j) FFT of the region shown in (i), with the corresponding reflections indexed as (20$\bar{1}$) and (060).

of the four irradiated regions (Figure S5c) displays a detectable D peak (Figure 3b), implying the limited sensitivity of Raman spectroscopy for identifying isolated defects in high-quality 2D materials with ultralow defect densities.

By contrast, Er-NP-enhanced PL mapping yields clear and reproducible fluorescence signals from all four laser-irradiated zones (Figure 3c), underscoring substantially improved defect-identification capability compared to traditional Raman spectroscopy.

Remarkably, the PL signal is confined to the irradiated areas, and its intensity shows a positive correlation with laser exposure dosage, consistent with enhanced Er-NP accumulation at higher defect densities (Figures S5d,e). These localized PL enhancement regions are assigned to nanoscale defect-related adsorption sites, whereas continuous line-like or spatially extended PL features are attributed to wrinkles, residues, or other topographic inhomogeneities and excluded from defect statistics (Figure S6).

We further construct extreme cases as additional references. By employing plasma hydrogen etching, we fabricate a graphene sample with an ultrahigh NPD density, and observe strong PL intensity across the entire mapped region, consistent with HRTEM characterization (Figure S7a–e). Conversely, no discernible PL signals appear on ultrahigh-quality graphene exfoliated from epitaxially grown single-crystal graphite after Er-NP deposition (Figure S7f–h) [46, 47].

The approach also enables robust identification of naturally occurring NPDs in commonly used 2D material samples. For Kish graphene over a typical area spanning tens of microns (Figure S8a,b), Raman spectra reveal only a weak D band slightly above the background noise level (Figures 3d and S8c), and many smaller or lower-density NPDs may remain undetected in the Raman mapping. By contrast, Er-NP-enhanced PL mapping reveals several additional defect-related hotspots (Figure 3e), owing to the higher SNR of Er-NP-based PL spectra compared with Raman signals (Figures 3f and S8d). HRTEM characterization further corroborates that $ErCl_3$ preferentially accumulates at defect sites to form nanoparticles and give rise to strong fluorescence signals (Figure 3g,h). Additionally, the magnified HRTEM image and the corresponding FFT reveal well-resolved lattice fringes with d spacings of 0.33 and 0.20 nm, corresponding to those of $(20\bar{1})$ and (060) planes for monoclinic $ErCl_3$ with space group C2/m (Figure 3i,j).

To further validate the utility of the approach, we fabricate field-effect transistor (FET) devices using graphene exfoliated from different bulk sources (e.g., Kish, EG, and HOPG), and measure carrier mobility under identical device architectures. We observe a negative correlation between the PL intensity per unit area and field-effect mobility, suggesting that higher PL emissions can reflect greater defect densities, indicating worse transport performance (Figure S9). This functional relationship between optical readout and electronic properties underscores the potential of our method as a powerful tool for evaluating 2D material quality.

Another key advantage of this method lies in its non-destructive nature. Due to the high volatility and low sublimation temperature of $ErCl_3$, the deposited fluorescent nanoparticles are readily evaporated and removed through an annealing process under UHV (Figure 4a). In practice, we perform in situ PL tracking in the same region of a graphene sample to confirm the efficiency and completeness of this removal process. After annealing, the previously strong and clearly distinguishable fluorescence signals completely vanish (Figures S10 and 4b–d), indicating that deposited Er-NPs can be cleanly removed without leaving residues or surface contaminants.

To rigorously assess whether the process affects the intrinsic structural integrity of the material, Raman spectra are recorded before Er-NP deposition and after removal. Comparative analysis shows no detectable changes in the peak positions, intensities, or full widths at half maximum (FWHM) of graphene's characteristic Raman peaks (G and 2D bands), indicating that the deposition/annealing cycle does not introduce additional structural defects or persistent dopants (Figure 4e). To further assess potential impacts on the electronic properties, FET devices are fabricated and electrically characterized using graphene from the same batch before and after the deposition/removal process. The measured carrier mobility exhibited only a negligible decrease of approximately 3.5% (from ~7 894 to ~7 613 $cm^2\ V^{-1}\ s^{-1}$), confirming the minimal impact and thus the non-destructive nature of the method (Figure 4f,g).

Finally, we further examine the universal practicality of this approach beyond graphene using hBN as another representative 2D material. Er-NPs deposited on hBN produce readily detectable fluorescence signals at defect-related sites, and these signals are completely eliminated after annealing without altering the intrinsic optical and structural properties of hBN (Figure S11). These results suggest that the Er-NP strategy is suitable for 2D materials with weak or absent intrinsic defect-related optical signatures, where sparse nanoscale defects are difficult to identify using conventional optical methods.

In conclusion, we develop and validate a rare-earth-assisted fluorescence method for identifying NPDs and assessing the quality of large-area 2D materials. Comprehensive theoretical calculations and experimental verification demonstrate that Er-NPs selectively deposit at NPD sites and generate high-contrast fluorescence signals, enabling rapid mapping of defect distributions. This method is especially advantageous for low-defect-density, optically inactive or weakly emissive systems such as high-quality graphene and hBN, and can serve as a complementary approach to Raman spectroscopy and atomic-resolution characterization techniques. Complete removal of Er-NPs by UHV annealing further ensures the non-destructive nature of the method. Overall, this work establishes an efficient strategy for high-throughput and high-sensitivity defect screening in high-quality large-area 2D materials, thereby facilitating their reliable transition from laboratory synthesis toward large-scale practical applications.

3 | Experimental Section

3.1 | DFT Calculations

Geometric optimization and energy calculations of the Er/graphene systems are carried out using density functional theory (DFT) as implemented in Vienna Ab initio Simulation Package. The generalized gradient approximation (GGA) with the Perdew–Burke–Ernzerhof (PBE) exchange-correlation function is used with the plane-wave cutoff energy set at 400 eV for all calculations. The dispersion-corrected DFT-D_3 method is used because of its good description of long-range vdW interactions for 2D materials. The geometries of the structures are relaxed until the force on each atom is less than 0.02 eV $Å^{-1}$,

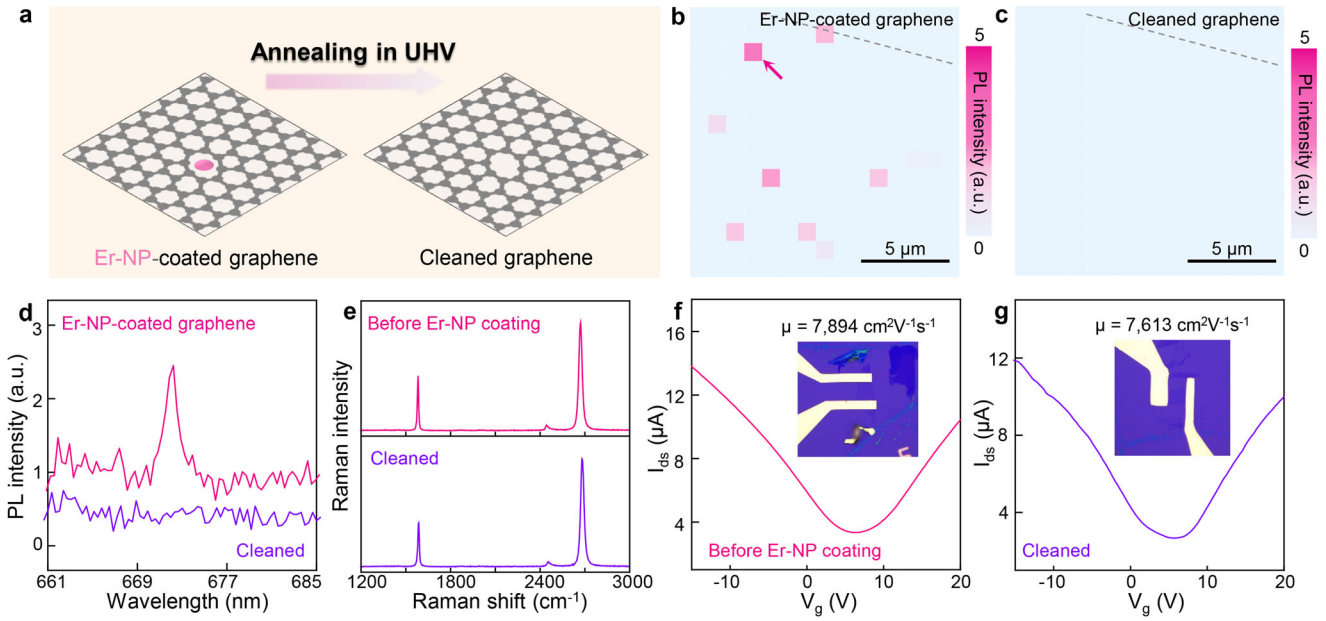

FIGURE 4 | Complete removal of Er-NPs enables non-destructive NPD characterization. (a) Schematic illustration of Er-NP removal from graphene by annealing under ultrahigh vacuum (UHV, 700°C for 3 h). (b,c) In situ PL mapping (672 nm) acquired from the same region before (b) Er-NP-coated graphene) and after (c) cleaned graphene) UHV annealing, showing the complete disappearance of defect-associated PL signals after removal. (d) Representative PL spectra collected at an NPD site before and after annealing, confirming the elimination of Er-related emission. (e) Raman spectra recorded before Er-NP deposition and after Er-NP removal, showing negligible changes in the G and 2D bands. (f,g) Electrical characterization of graphene FETs fabricated from the same batch: a reference device is measured without Er-NPs (f), while a separate device is fabricated and measured after Er-NP deposition and UHV annealing (g), because Au electrodes cannot tolerate the annealing; the extracted mobilities show only a marginal change (insets: optical images of the corresponding devices).

and the energy convergence criterion of 1×10^{-4} eV is met. The graphene surfaces are modelled by a periodic slab. The binding energies of the Er/graphene systems, namely, $\Delta E = (E_{total} - E_{gra} - n_{Er} \times u_{Er})/n_{Er}$, are calculated using the relaxed structures, where E_{total} is the total energy of the Er/graphene systems; E_{gra} is the energy of the graphene systems with vacancies; n_{Er} and u_{Er} represent the number and chemical potentials of Er atoms, respectively.

3.2 | Preparation of Samples

Kish graphene, EG graphene, and hBN domains are peeled off from Kish graphite (Grade 300, Graphene Supermarket), EG graphite (graphite grown by isothermal dissolution—diffusion—precipitation method in our group), and hBN crystals (Shanghai Onway Technology) onto Si/SiO_2 substrates through a Scotch-tape mechanical exfoliation process, respectively. The prepared Kish graphene samples are exposed to H_2 plasma radiation for 1 s duration to introduce high-density defects.

3.3 | Depositing Process of Er-NPs

The prepared 2D material samples and 21 mg of $ErCl_3$ powder are placed in a high-temperature tube furnace. In this setup, the $ErCl_3$ powder is positioned upstream in the furnace, while the 2D material samples are located downstream. An inert protective gas Ar is introduced at a flow rate of 40 sccm while maintaining a low pressure within the tube. The furnace upstream is set at 900°C to evaporate the $ErCl_3$ powder and deposit it onto the 2D material samples, forming Er-NPs.

3.4 | Annealing Process of Er-Deposited Samples

The Er-NP-deposited samples are subjected to an annealing process at 700°C for a 3 h duration to entirely remove adsorbed Er-NPs on the surface of the samples.

3.5 | Characterizations

Optical images were acquired using an Olympus BX51M microscope. Raman spectra, PL spectra, and corresponding mappings were collected using the same custom-designed optical system with an excitation wavelength of 514 nm. The Raman and PL mapping parameters (10 mW excitation power, 5 s integration time per pixel, and a step size of 1 μm) were selected after systematic optimization of excitation power and integration time to balance defect detectability and practical large-area mapping efficiency. TEM experiments are performed using an FEI Titan Themis G2 300 instrument operated at 300 kV.

3.6 | Electric Device Fabrication and Measurement

The monolayer graphene is exfoliated from Kish graphite and EG graphite onto the SiO_2/Si substrate (300 nm of SiO_2). Then,

a two-contact-shaped mask is defined on the location of the graphene sample by electron-beam lithography of a polymethyl methacrylate resist. Afterwards, we deposited metal leads (5 nm Cr/50 nm Au) by electron-beam evaporation to make an electrical contact. Finally, two-terminal FET transport measurements are performed using the semiconductor analyser (Keysight B1500A) at room temperature in a high vacuum environment.

Author Contributions

L.W. conceived the experiment and supervised the project. T.L. performed the main experiment and characterizations. W.W. contributed to the theoretical calculation. M.D. and Z.Z. performed the electrical measurement. P.W., R.Q., Q.G., and X.B. conducted the electron microscopy characterizations. M.Z., Y.P., C.L., and X.X. helped with the sample growth in this work. H.H. and K.L. assisted in optical measurements in this work.

Acknowledgements

This work is supported by the National Key Research and Development Program of China (2023YFB4603603, 2024YFF0508502, 2024YFA1409600), the National Natural Science Foundation of China (T2422029, 52272173, 52402043, 12274456, 52302183, 12334001, 52427802, 42550189, 92577201, U24A20285, 12404209), the Natural Science Foundation of Jiangsu Province (BK20230896), the Research Fund of State Key Laboratory of Mechanics and Control for Aerospace Structures (Nanjing University of Aeronautics and Astronautics, MCAS-I-0525K01), the Qiushi Academic Project of Renmin University of China (RUC25QSDL129), the Beijing Natural Science Foundation (JQ26013), the Scientific Research Innovation Capability Support Project for Young Faculty (SRICSPYF-BS2025136), the Guangdong Provincial Science Fund for Distinguished Young Scholars (2026B1515020003). L.W. is grateful for the support from the Youth Innovation Promotion Association of CAS.

Conflicts of Interest

The authors declare no conflict of interest.

Data Availability Statement

The data that support the findings of this study are available from the corresponding author upon reasonable request.

References

1. M. Q. Zeng, Y. Xiao, J. X. Liu, K. N. Yang, and L. Fu, "Exploring Two-Dimensional Materials Toward the Next-Generation Circuits: From Monomer Design to Assembly Control," *Chemical Reviews* 118 (2018): 6236–6296, https://doi.org/10.1021/acs.chemrev.7b00633.

2. D. Akinwande, C. Huyghebaert, C.-H. Wang, et al., "Graphene and Two-Dimensional Materials for Silicon Technology," *Nature* 573 (2019): 507–518, https://doi.org/10.1038/s41586-019-1573-9.

3. K. Zhu, C. Wen, A. A. Aljarb, et al., "The Development of Integrated Circuits Based on Two-Dimensional Materials," *Nature Electronics* 4 (2021): 775–785, https://doi.org/10.1038/s41928-021-00672-z.

4. B. Qin, C. Ma, Q. Guo, et al., "Interfacial Epitaxy of Multilayer Rhombohedral Transition-Metal Dichalcogenide Single Crystals," *Science* 385 (2024): 99–104, https://doi.org/10.1126/science.ado6038.

5. L. Wang, J. Qi, W. Wei, et al., "Bevel-Edge Epitaxy of Ferroelectric Rhombohedral Boron Nitride Single Crystal," *Nature* 629 (2024): 74–79, https://doi.org/10.1038/s41586-024-07286-3.

6. V. L. Nguyen, B. G. Shin, D. L. Duong, et al., "Seamless Stitching of Graphene Domains on Polished Copper (111) Foil," *Advanced Materials* 27 (2015): 1376–1382, https://doi.org/10.1002/adma.201404541.

7. X. Xu, Z. Zhang, J. Dong, et al., "Ultrafast Epitaxial Growth of Metre-Sized Single-Crystal Graphene on Industrial Cu Foil," *Science Bulletin* 62 (2017): 1074–1080, https://doi.org/10.1016/j.scib.2017.07.005.

8. L. Wang, X. Xu, L. Zhang, et al., "Epitaxial Growth of a 100-Square-Centimetre Single-Crystal Hexagonal Boron Nitride Monolayer on Copper," *Nature* 570 (2019): 91–95, https://doi.org/10.1038/s41586-019-1226-z.

9. J. Wang, X. Xu, T. Cheng, et al., "Dual-Coupling-Guided Epitaxial Growth of Wafer-Scale Single-Crystal WS_2 Monolayer on Vicinal a-Plane Sapphire," *Nature Nanotechnology* 17 (2022): 33–38, https://doi.org/10.1038/s41565-021-01004-0.

10. A. M. Van Der Zande, P. Y. Huang, D. A. Chenet, et al., "Grains and Grain Boundaries in Highly Crystalline Monolayer Molybdenum Disulphide," *Nature Materials* 12 (2013): 554–561, https://doi.org/10.1038/nmat3633.

11. J. Cheng, D. Huang, T. Jiang, et al., "Chiral Selection Rules for Multi-Photon Processes in Two-Dimensional Honeycomb Materials," *Optics Letters* 44 (2019): 2141–2144, https://doi.org/10.1364/OL.44.002141.

12. L. Zhou, H. Fu, T. Lv, et al., "Nonlinear Optical Characterization of 2D Materials," *Nanomaterials* 10 (2020): 2263, https://doi.org/10.3390/nano10112263.

13. H. I. Rasool, C. Ophus, and A. Zettl, "Atomic Defects in Two Dimensional Materials," *Advanced Materials* 27 (2015): 5771–5777, https://doi.org/10.1002/adma.201500231.

14. J. H. Hong, C. H. Jin, J. Yuan, and Z. Zhang, "Atomic Defects in Two-Dimensional Materials: From Single-Atom Spectroscopy to Functionalities in Opto-/Electronics, Nanomagnetism, and Catalysis," *Advanced Materials* 29 (2017): 1606434, https://doi.org/10.1002/adma.201606434.

15. A. Hashimoto, K. Suenaga, A. Gloter, K. Urita, and S. Iijima, "Direct Evidence for Atomic Defects in Graphene Layers," *Nature* 430 (2004): 870–873, https://doi.org/10.1038/nature02817.

16. M. H. Gass, U. Bangert, A. L. Bleloch, P. Wang, R. R. Nair, and A. K. Geim, "Free-Standing Graphene at Atomic Resolution," *Nature Nanotechnology* 3 (2008): 676–681, https://doi.org/10.1038/nnano.2008.280.

17. H. Qiu, T. Xu, Z. Wang, et al., "Hopping Transport Through Defect-Induced Localized States in Molybdenum Disulphide," *Nature Communications* 4 (2013): 2642, https://doi.org/10.1038/ncomms3642.

18. W. Zhou, X. Zou, S. Najmaei, et al., "Intrinsic Structural Defects in Monolayer Molybdenum Disulfide," *Nano Letters* 13 (2013): 2615–2622, https://doi.org/10.1021/nl4007479.

19. J. Hong, Z. Hu, M. Probert, et al., "Exploring Atomic Defects in Molybdenum Disulphide Monolayers," *Nature Communications* 6 (2015): 6293, https://doi.org/10.1038/ncomms7293.

20. J. Zhang, Y. Yu, P. Wang, et al., "Characterization of Atomic Defects on the Photoluminescence in Two-Dimensional Materials Using Transmission Electron Microscope," *InfoMat* 1 (2019): 85–97, https://doi.org/10.1002/inf2.12002.

21. J. Zhang, R. Sun, D. Ruan, et al., "Point Defects in Two-Dimensional Hexagonal Boron Nitride: A Perspective," *Journal of Applied Physics* 128 (2020): 100902, https://doi.org/10.1063/5.0021093.

22. D. Wong, J. Velasco, L. Ju, et al., "Characterization and Manipulation of Individual Defects in Insulating Hexagonal Boron Nitride Using Scanning Tunnelling Microscopy," *Nature Nanotechnology* 10 (2015): 949–953, https://doi.org/10.1038/nnano.2015.188.

23. Y. Zhang, S.-Y. Li, H. Huang, et al., "Scanning Tunneling Microscopy of the π Magnetism of a Single Carbon Vacancy in Graphene," *Physical Review Letters* 117 (2016): 166801, https://doi.org/10.1103/PhysRevLett.117.166801.

24. P. Vancsó, G. Z. Magda, J. Peto, et al., "The Intrinsic Defect Structure of Exfoliated MoS_2 Single Layers Revealed by Scanning Tunneling Microscopy," *Scientific Reports* 6 (2016): 29726, https://doi.org/10.1038/srep29726.

25. S. S. Wang, A. Robertson, and J. H. Warner, "Atomic Structure of Defects and Dopants in 2D Layered Transition Metal Dichalcogenides," *Chemical Society Reviews* 47 (2018): 6764–6794, https://doi.org/10.1039/c8cs00236c.

26. K. Zhussupbekov, L. Ansari, J. B. McManus, et al., "Imaging and Identification of Point Defects in $PtTe_2$," *NPJ 2D Materials and Applications* 5 (2021): 14, https://doi.org/10.1038/s41699-020-00196-8.

27. M. R. Rosenberger, H.-J. Chuang, K. M. McCreary, C. H. Li, and B. T. Jonker, "Electrical Characterization of Discrete Defects and Impact of Defect Density on Photoluminescence in Monolayer WS_2," *ACS Nano* 12 (2018): 1793–1800, https://doi.org/10.1021/acsnano.7b08566.

28. L. G. Cançado, A. Jorio, E. M. Ferreira, et al., "Quantifying Defects in Graphene via Raman Spectroscopy at Different Excitation Energies," *Nano Letters* 11 (2011): 3190–3196, https://doi.org/10.1021/nl201432g.

29. A. Eckmann, A. Felten, A. Mishchenko, et al., "Probing the Nature of Defects in Graphene by Raman Spectroscopy," *Nano Letters* 12 (2012): 3925–3930, https://doi.org/10.1021/nl300901a.

30. S. Mignuzzi, A. J. Pollard, N. Bonini, et al., "Effect of disorder on Raman Scattering of Single-Layer MoS_2," *Physical Review B* 91 (2015): 195411, https://doi.org/10.1103/PhysRevB.91.195411.

31. P. K. Chow, R. B. Jacobs-Gedrim, J. Gao, et al., "Defect-Induced Photoluminescence in Monolayer Semiconducting Transition Metal Dichalcogenides," *ACS Nano* 9 (2015): 1520–1527, https://doi.org/10.1021/nn5073495.

32. Y. Lee, S. Park, H. Kim, G. H. Han, Y. H. Lee, and J. Kim, "Characterization of the Structural Defects in CVD-Grown Monolayered MoS_2 Using Near-Field Photoluminescence Imaging," *Nanoscale* 7 (2015): 11909–11914, https://doi.org/10.1039/c5nr02897c.

33. T. T. Tran, K. Bray, M. J. Ford, M. Toth, and I. Aharonovich, "Quantum Emission From Hexagonal Boron Nitride Monolayers," *Nature Nanotechnology* 11 (2016): 37–41, https://doi.org/10.1038/nnano.2015.242.

34. H. G. Rosa, L. Junpeng, L. C. Gomes, M. J. L. F. Rodrigues, S. C. Haur, and J. C. V. Gomes, "Second-Harmonic Spectroscopy for Defects Engineering Monitoring in Transition Metal Dichalcogenides," *Advanced Optical Materials* 6 (2018): 1701327, https://doi.org/10.1002/adom.201701327.

35. T. H. Ly, M.-H. Chiu, M.-Y. Li, et al., "Observing Grain Boundaries in CVD-Grown Monolayer Transition Metal Dichalcogenides," *ACS Nano* 8 (2014): 11401–11408, https://doi.org/10.1021/nn504470q.

36. S. Wu, R. Yang, D. X. Shi, and G. Y. Zhang, "Identification of Structural Defects in Graphitic Materials by Gas-Phase Anisotropic Etching," *Nanoscale* 4 (2012): 2005–2009, https://doi.org/10.1039/c2nr11707j.

37. M. Yamamoto, T. L. Einstein, M. S. Fuhrer, and W. G. Cullen, "Anisotropic Etching of Atomically Thin MoS_2," *Journal of Physical Chemistry C* 117 (2013): 25643–25649, https://doi.org/10.1021/jp410893e.

38. Y. Zhang, H. Zhang, F. Li, et al., "Invisible Growth of Microstructural Defects in Graphene Chemical Vapor Deposition on Copper Foil," *Carbon* 96 (2016): 237–242, https://doi.org/10.1016/j.carbon.2015.09.041.

39. Y. Ryu, W. Kim, S. Koo, et al., "Interface-Confined Doubly Anisotropic Oxidation of Two-Dimensional MoS_2," *Nano Letters* 17 (2017): 7267–7273, https://doi.org/10.1021/acs.nanolett.7b02621.

40. Y. Guo, Q. Wang, X. Li, et al., "Direct Visualization of Structural Defects in 2D Semiconductors," *Chinese Physics B* 31 (2022): 076105, https://doi.org/10.1088/1674-1056/ac6738.

41. J.-H. Son, S.-J. Baeck, M.-H. Park, et al., "Detection of Graphene Domains and Defects Using Liquid Crystals," *Nature Communications* 5 (2014): 3484, https://doi.org/10.1038/ncomms4484.

42. M. Zhang, M. Lihter, T.-H. Chen, et al., "Super-Resolved Optical Mapping of Reactive Sulfur-Vacancies in Two-Dimensional Transition Metal Dichalcogenides," *ACS Nano* 15 (2021): 7168–7178, https://doi.org/10.1021/acsnano.1c00373.

43. F. Banhart, J. Kotakoski, and A. V. Krasheninnikov, "Structural Defects in Graphene," *ACS Nano* 5 (2011): 26–41, https://doi.org/10.1021/nn102598m.

44. E. J. Duplock, M. Scheffler, and P. J. Lindan, "Hallmark of Perfect Graphene," *Physical Review Letters* 92 (2004): 225502, https://doi.org/10.1103/PhysRevLett.92.225502.

45. R. Sekar, A. Ravitchandiran, and S. Angaiah, "Recent Advances and Challenges in Light Conversion Phosphor Materials for Third-Generation Quantum-Dot-Sensitized Photovoltaics," *ACS Omega* 7 (2022): 35351–35360, https://doi.org/10.1021/acsomega.2c03736.

46. Z. Zhang, M. Ding, T. Cheng, et al., "Continuous Epitaxy of Single-Crystal Graphite Films by Isothermal Carbon Diffusion Through Nickel," *Nature Nanotechnology* 17 (2022): 1258–1264, https://doi.org/10.1038/s41565-022-01230-0.

47. M. Ding, Z. Zhang, W. Wei, et al., "Ultrapure Graphite From Solid Refining," *Advanced Materials* 37 (2025): 2500461, https://doi.org/10.1002/adma.202500461.

Supporting Information

Additional supporting information can be found online in the Supporting Information section.

Supporting File: adma74351-sup-0001-SuppMat.pdf.